

This document is confidential and is proprietary to the American Chemical Society and its authors. Do not copy or disclose without written permission. If you have received this item in error, notify the sender and delete all copies.

**Probing the Role of Internalized Geometric Strain on  
Heterogeneous Electrocatalysis**

Journal:	<i>Chemistry of Materials</i>
Manuscript ID	cm-2019-02234n.R1
Manuscript Type:	Article
Date Submitted by the Author:	n/a
Complete List of Authors:	Alsac, Elif Pinar; University of Waterloo, Chemistry Whittingham, Alexander; University of Waterloo, Chemistry Liu, Yutong; University of Waterloo, Chemistry Smith, Rodney; University of Waterloo, Chemistry

SCHOLARONE™  
Manuscripts

1  
2  
3  
4  
5  
6  
7  
8  
9  
10  
11  
12  
13  
14  
15  
16  
17  
18  
19  
20  
21  
22  
23  
24  
25  
26  
27  
28  
29  
30  
31  
32  
33  
34  
35  
36  
37  
38  
39  
40  
41  
42  
43  
44  
45  
46  
47  
48  
49  
50  
51  
52  
53  
54  
55  
56  
57  
58  
59  
60

**Probing the Role of Internalized Geometric Strain on Heterogeneous Electrocatalysis**

Elif Pınar Alsaç, Alexander Whittingham, Yutong Liu, Rodney D. L. Smith\*

*Department of Chemistry, University of Waterloo*  
*200 University Avenue W., Waterloo, Ontario, Canada N2L 3G1*

*Correspondence to:*  
rodsmith@uwaterloo.ca

## Summary

The chemistry underlying the activation of nickel hydroxide towards electrocatalytic oxygen evolution by incorporation of iron remains the subject of debate. We extract insights into the role of geometric strain on the electrochemical behavior in this class of materials by blending aluminum, gallium or iron into a disordered nickel hydroxide lattice. The electrochemical behavior and electronic structure of the three binary composition series are found to be similarly influenced by each additive cation. Density functional theory models indicate that the additive cations asymmetrically impede the voltage-induced expansion and contraction of the nickel hydroxide host lattice, a feature that is supported by near infrared spectroscopy. Reaction coordinate diagrams suggest that this distortion decreases the activation energy for electron transfer by decreasing the extent to which the lattice can expand and contract, but that iron is unique in its ability to favor oxidation by distorting the shape of the potential energy surface of the oxidized state to lower the electron transfer coefficient. These results reveal that interference with voltage-induced structural changes by incorporation of suitably sized ions alters the electrochemical behavior, but that overall electrocatalytic performance cannot be linearly controlled by such geometric distortions.

## INTRODUCTION

Efforts to understand and improve the performance of heterogeneous electrocatalysts have traditionally focused on the composition of the solid-state catalyst materials. A correlation between the binding energies of reaction intermediates and catalyst performance is firmly established for materials with well-defined structures.<sup>1–3</sup> Such correlations have enabled optimization of catalyst compositions for families of solid-state electrocatalysts for the oxygen evolution reaction (OER) by considering chemical descriptors such as the experimentally measured population of antibonding orbitals in perovskite crystals<sup>4</sup> or the computationally predicted binding energy of intermediates.<sup>5</sup> The volcano-plots that arise from such studies can be effective catalyst design tools, but they rely on assumptions that the catalyst structure and reaction mechanism do not change during catalysis. Further, computationally predicted energetics require a clearly defined bonding framework for the catalyst material. The performance of disordered or amorphous phases for OER electrocatalysis,<sup>6,7</sup> the experimental observation of both reversible and irreversible phase changes during catalyst operation,<sup>8–10</sup> the unexpected identification of basal-plane MoS<sub>2</sub> vacancies as highly active reaction sites,<sup>11</sup> and the prediction of situations where the underlying assumptions are expected to fail<sup>2</sup> all highlight the limits of such an approach. Geometric strain within solid-state structures is emerging as an alternative means to influence the behavior and performance of electrocatalysts. Functional examples of “strain engineering” have improved understanding of the effects of strain on electronic structure and electrochemical behavior,<sup>11–18</sup> to the point that proposals to parametrize strain as a predictor for electrocatalytic performance have been made.<sup>19</sup> The success of such an approach raises questions regarding the relative importance of strain on the geometric and electronic structure in known catalysts. We address this question here for disordered nickel (oxy)hydroxide electrocatalysts.

The incorporation of iron ions into nickel hydroxide converts a poor OER catalyst into one of the best known. This transition is characterized by an anodic shift in pre-catalytic redox peaks, a cathodic shift in the onset of electrocatalytic OER, and an increased responsiveness of the catalyst to increased overpotentials.<sup>20–24</sup> The chemistry underlying this transition remains a topic of debate; prominent recent proposals have ascribed catalytic performance gains to the presence of coordination environments that enable direct oxidation of Fe-based reaction sites,<sup>25,26</sup> or to the activation Ni-based reaction sites by Fe ions.<sup>27,28</sup> Numerous studies provide support for each of the above proposals by providing evidence that that Fe ions either are,<sup>29,30</sup> or are not,<sup>31–33</sup> electrochemically oxidized under catalytic conditions. The literature surrounding these mechanistic proposals thus provides little conclusive evidence for the validity of any single proposal.

Herein, we explore the impact of internalized geometric strain on electrochemical behavior by blending trivalent cations into a host nickel hydroxide lattice. The electronic structure and electrochemical behavior of Al-Ni, Ga-Ni and Fe-Ni binary composition series are found to correlate to the effective ionic radius of the secondary cation. We confirm composition-dependent structural distortions in all three of the composition series by tracking *d-d* transitions with near infrared (NIR) spectroscopy and utilize density functional theory (DFT) to gain mechanistic insight. The precatalytic behavior is affected in an identical way for all composition series, but only Fe affords significant improvements in catalytic performance.

## EXPERIMENTAL

**Materials.** Nickel(II) 2-ethylhexanoate (78% in 2-ethylhexanoic acid, Strem Chemicals Inc.), iron (III) 2-ethylhexanoate (6% solution in mineral spirits, Strem Chemicals Inc.), aluminum (III) 2,4-pentanedionate (Alfa Aesar) and gallium (III) acetylacetonate (99.99%, Sigma-Aldrich), indium (III) acetylacetonate (98%, Alfa Aesar) and indium (III) acetate (99.99%, Alfa Aesar) were used as received. Fluorine-doped tin oxide glass (FTO; TEC-7 grade, Hartford Glass) was cleaned immediately prior to use by sequential ultrasonication in a detergent solution, milli-Q H<sub>2</sub>O, then isopropanol. The surface was dried under a stream of N<sub>2</sub> and placed in a custom UV-irradiation chamber (GHO18T5VH lamp, Atlantic Ultraviolet) for 15 minutes. Aqueous 1 M KOH solutions were prepared using milli-Q H<sub>2</sub>O and reagent grade KOH (>85%, Sigma-Aldrich). Iron impurities were removed from these electrolyte solutions by aging over Ni(OH)<sub>2</sub>, as previously described.<sup>22</sup> Catalyst films were fabricated by dissolving precursor complexes in ethanol with the relevant stoichiometry and a total metal concentration of 0.3 M. The solutions were spin-coated onto freshly cleaned FTO and placed in a UV-irradiation chamber for 24 hours.<sup>6,28</sup> Attempts to synthesize nickel-indium compositions were unsuccessful due to the insolubility of indium compounds in solvents suitable for spin coating precursor films.

**Electrochemistry.** All experiments were carried out with 1 M KOH electrolyte solutions in a single-compartment polyethylene cell. A Bio-logic SP-300 was used in conjunction with a Gaskatel HydroFlex Reversible Hydrogen Electrode (RHE) as the reference electrode, a platinum mesh as the counter electrode, and catalyst-coated FTO as working electrodes. Cyclic voltammetry experiments consisted of 5 cycles between 0.9 and 1.7 V vs. RHE at a rate of 1 mV s<sup>-1</sup>. Reproducible voltammograms were obtained after 2 or 3 cycles; data shown represents the stabilized behavior. Electron transfer kinetics were measured by a chronoamperometry experiments in both the anodic and cathodic directions. The voltage was stepped from 0.9 to 1.7 V vs. RHE in 10 mV, 60 second steps. The current density at the end of each step was taken as the steady-state catalytic current. Cell resistances were measured by impedance spectroscopy prior to electrochemical experiments, with values on the order of 15 Ohms measured for all samples. All experiments were performed without resistance correction; the voltage axis of Tafel plots were corrected for resistance ( $E = E_{\text{Ref}} - iR_u$ ).

**Infrared Spectroscopy.** Spectroscopic measurements were performed on a Nicolet 6700 FTIR equipped with a Pike Technologies VeeMAX III variable angle reflection accessory. An InGaAs detector and a white light source were used to acquire near-infrared spectra on all samples. Spectra from 4000 to 800 cm<sup>-1</sup> were recorded on a subset of samples using a DTGS detector with an infrared light source. Spectra were acquired from 8000 to 2500 cm<sup>-1</sup> on this subset samples with a white light source and DTGS detector to ensure accurate comparison between the mid- and near-infrared regions (see online Supplementary Information). Samples were prepared by maintaining a voltage of either 1.6 V vs. RHE (oxidized) or 0.9 V vs. RHE (reduced) for 10 minutes. Electrodes were then removed from solution, excess electrolyte solution was removed from the surface using compressed nitrogen, and the spectra were acquired with an incident angle of 30°. A clean piece of FTO served as the baseline for all spectra. Peak locations were extracted by fitting the spectra with 3 Gaussian shaped peaks. All spectra and a sample of the fitted peaks are available in the online Supplementary Information.

**X-ray Photoelectron Spectroscopy.** Measurements were performed on a Thermo-VG Scientific ESCALab 250 microprobe using a magnesium X-ray source. Survey scans were performed using a pass energy of 50 eV and high-resolution scans with 30 eV. All measurements were performed on films

deposited on FTO glass with a small strip of conductive carbon tape to make electrical contact. Films that were employed for electrochemical experiments were thoroughly rinsed with milliQ H<sub>2</sub>O and allowed to air dry before loading into the sample chamber. Argon sputtering was performed for a period of 600 seconds. Quantification was performed on the high-resolution scans using CasaXPS and the following relative scaling factors (r.s.f.). The 20% Ga sample was analyzed using the Ni 2*p* (r.s.f. = 13.92 and 7.18 for 2*p*<sub>3/2</sub> and 2*p*<sub>1/2</sub>) and Ga 2*p* (20.47 and 10.56 for 2*p*<sub>3/2</sub> and 2*p*<sub>1/2</sub>) regions. Overlap of Al and Ni-based photoelectrons in the 20% Al required deconvolution of the Al 2*p* (0.5735) and Ni 3*p* (1.36 and 0.701 for 3*p*<sub>3/2</sub> and 3*p*<sub>1/2</sub>) features. The area of the Ni 3*p*<sub>1/2</sub> component was constrained to be half that of the Ni 3*p*<sub>3/2</sub> component during deconvolution. Argon-sputtering of 20% Al sample that was electrochemically conditioned induced a change in speciation of the nickel within the film (Figure S3D and S3E), necessitating the use of four peaks to describe the Ni 3*p* component. Spectra were calibrated by shifting the adventitious carbon 1*s* peak to 285.0 eV.

**Density Functional Theory.** Calculations were performed with plane-wave based density functional theory (DFT) in the Quantum ESPRESSO package.<sup>34</sup> The pre-catalytic process was shown to be a Ni<sup>IV/II</sup> transition for materials related to those studied here.<sup>28</sup> Structural models were therefore chosen as [Ni<sub>9</sub>(OH)<sub>18</sub>] and [Ni<sub>9</sub>O<sub>18</sub>] for the pure nickel composition and [M<sub>1</sub>Ni<sub>8</sub>O(OH)<sub>17</sub>] and [M<sub>1</sub>Ni<sub>8</sub>O<sub>18</sub>]<sup>-</sup> for the Al<sup>III</sup>, Ga<sup>III</sup> and Fe<sup>III</sup> containing materials. Relaxations of periodic slabs were initiated using a single 2-dimensional sheet of β-Ni(OH)<sub>2</sub> containing nine cations and 15 Å of vacuum between layers. Projector augmented wave pseudopotentials with PBE exchange correlated functionals were used with plane-wave cutoff values of 50 Ry and 500 Ry. A 10x10x1 Monkhorst-Pack grid was employed, with Hubbard-U terms fixed at 6.6 eV for Ni and 3.5 eV for Fe to maintain consistency with past reports.<sup>25,30</sup> The in-plane unit cell dimension was systematically increased relative to β-NiOOH to model tensile strain on the oxidized phases, or decreased relative to β-Ni(OH)<sub>2</sub> to introduce compressive strain on the reduced phases. Each series of calculations involved 8 distinct calculations with a fixed unit cell, from 0 to 7% strain, and one with a variable unit cell. The computationally predicted *R*<sub>Ni-M</sub> distances (optimized structures available in Supplementary Information) are slightly larger than experimentally measured values for the reduced phase and smaller for the oxidized phase.<sup>28</sup> We therefore limit ourselves to a qualitative analysis of trends as rigorously accurate structural models are impossible for the disordered material being studied here.

## RESULTS

Three series of thin films based on the formula M<sub>y</sub>Ni<sub>100-y</sub>O<sub>x</sub> were fabricated, where the nominal *y* was varied from 0 to 30 in steps of 5 and *M* is Al<sup>III</sup>, Ga<sup>III</sup> or Fe<sup>III</sup>. These additive elements were chosen using selection criteria intended to isolate and explore the role of geometric strain on the electrochemical behavior of nickel hydroxide. The selection criteria were that each element must be known to (i) be compatible with layered double hydroxide phases,<sup>35–37</sup> (ii) provide a gradient in effective ionic radii that resides between those for Ni<sup>II</sup> and Ni<sup>IV</sup>,<sup>38</sup> (iii) have equivalent electrostatic charge, and (iv) offer no standard reduction potential in the voltage range of interest. Experimental evidence for the electrochemical oxidation of Fe<sup>III</sup> to higher oxidation states has been reported for related materials,<sup>26,29,39</sup> but such observations were at voltages above the anodic voltage limit employed here. Uniform films of these materials were fabricated on FTO substrates by spin-coating a solution of photochemically reactive precursors containing the desired molar stoichiometry, then irradiating the precursor film with UV-light. This fabrication protocol yields films with a highly disordered structure that are *ca.* 150 nm

thick. X-ray diffraction has been shown to be ineffective in characterizing these materials,<sup>6,20</sup> but X-ray absorption spectroscopy indicates a disordered structure related to layered doubly hydroxides in which all nickel sites are electrochemically accessible.<sup>28</sup> These films have been shown achieve complete coverage and be highly uniform in their as-deposited state, with morphological changes yielding increased surface roughness after electrochemical testing.<sup>20</sup>

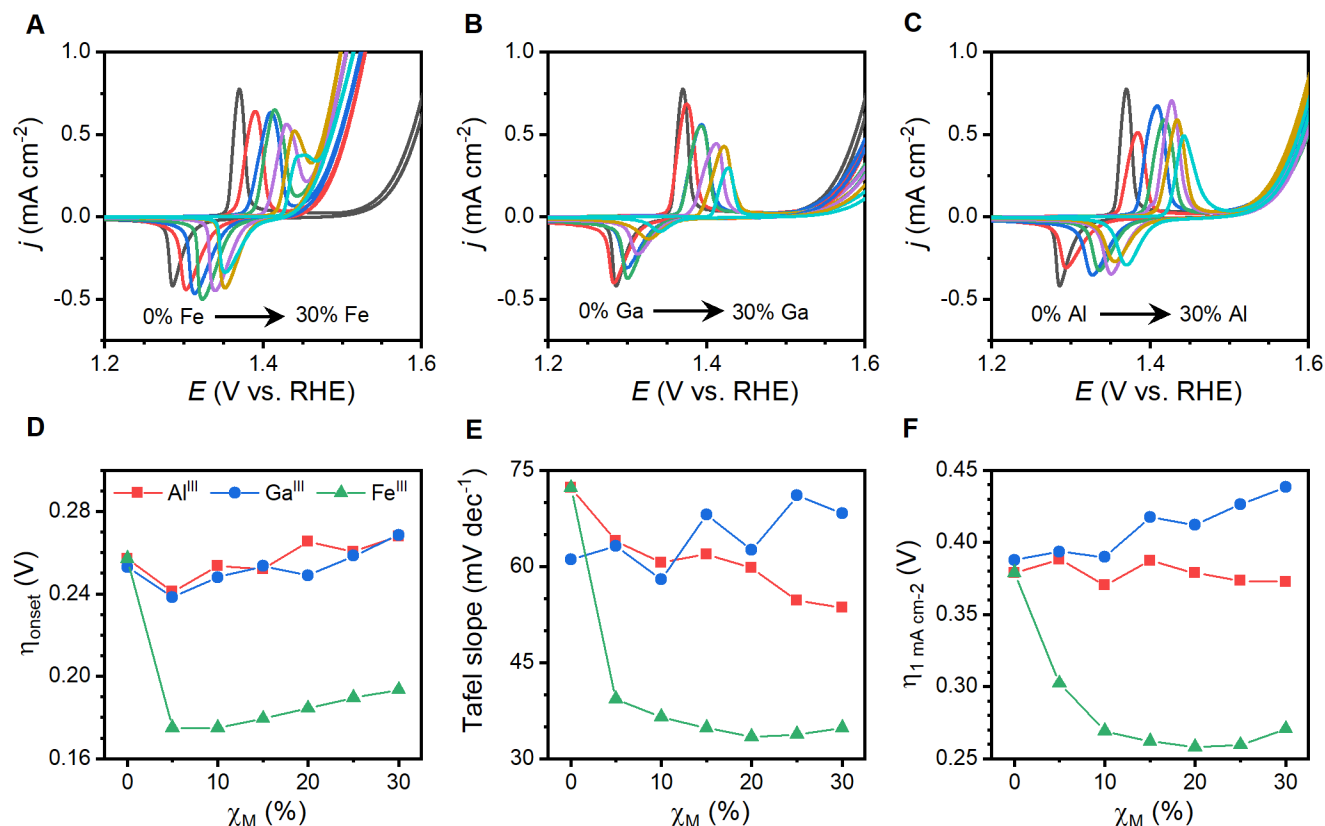


**Figure 1.** Electrochemical behavior of the three  $M_yNi_{100-y}O_x$  composition series. Cyclic voltammograms acquired for 5% relative stoichiometry steps in the (A) Fe-Ni, (B) Ga-Ni and (C) Al-Ni composition series. The (D) catalytic onset, (E) Tafel slope and (F) overpotential to reach 1 mA cm<sup>-2</sup> are plotted as a function of composition for Fe-Ni (green triangles), Ga-Ni (blue circles) and Al-Ni (red squares).

Voltammetric characterization of the Al-Ni, Ga-Ni and Fe-Ni composition series reveal identical trends in pre-catalytic behavior but disparate electrocatalytic performance (Figures 1 and S1). A pre-catalytic redox process decreases in size and shifts anodically at a rate of 2.5 mV per percent addition of Fe in the Fe-Ni series. The pre-catalytic redox process is variably assigned to a  $Ni^{II}$  to  $Ni^{III}$ ,<sup>21,22,40</sup> or a  $Ni^{II}$  to  $Ni^{IV}$  transition for nickel oxyhydroxides,<sup>28,33</sup> likely owing to differences in fabrication and characterization protocols. We assign a  $Ni^{II}$  to  $Ni^{IV}$  transition as indicated by a recent analysis of photochemically deposited  $Fe_yNi_{100-y}O_x$ .<sup>28</sup> The subsequent exponential rise in currents is electrocatalytic OER. This feature exhibits a significant cathodic shift following addition of Fe, with the majority of the shift occurring within the first 5% Fe addition. This behavior is characteristic of the material and is in agreement with all past studies on iron-nickel (oxy)hydroxides.<sup>21,22,28</sup> The pre-catalytic redox process for both Ga-Ni and Al-Ni series exhibits a 2.6 mV anodic shift per percent of additional metal, but no clear catalytic gains as seen in the Fe-Ni series. The well-defined pre-catalytic redox peaks observed for all three composition series show no signs of shouldering or peak-splitting, suggesting a homogeneous

distribution of the dopant cations. The identical behavior of the pre-catalytic redox process in all composition series suggests preservation of the nature of the pre-catalytic electron transfer process despite differences between the additive elements. Incorporation of iron into nickel hydroxide yields the characteristic changes in electrocatalytic OER: a sudden decrease in the onset overpotential for electrocatalytic OER ( $\eta_{\text{onset}}$ ; Figure 1D), defined here as the onset of linearity in Tafel plot, and a stepped decrease in the measured Tafel slope (Figure 1E). This overall behavior is in excellent agreement with that previously reported for the Fe-Ni composition series deposited on glassy carbon electrodes,<sup>28</sup> suggesting that no electrode substrate effects are at play. Neither of these characteristic changes is observed for the Al-Ni or Ga-Ni composition series, where the Tafel slopes gradually change by *ca.* 10 mV dec<sup>-1</sup> and  $\eta_{\text{onset}}$  slightly increases. The differences in electrocatalytic behavior observed here (Figure S2) supports the assertion that electrocatalytic OER and the pre-catalytic process are fundamentally decoupled and not a linear series of events.

The surface compositions of the 20% Ga and 20% Al samples were examined by X-ray photoelectron spectroscopy (XPS) before and after electrochemical testing. High resolution XPS scans in the Fe 2*p* region show no Fe in either sample (Figure S3). A single peak is observed in this region for each sample, but the singlet structure, a 715.6 eV binding energy and the presence of a second peak at 758.0 eV in the survey scan enable assignment of this peak to a Sn 3*p* emission from exposed fluorine-doped tin oxide substrate. Emergence of this peak is consistent with the morphological changes known to occur in these materials.<sup>20</sup> Evidence that changes observed in electrochemical behavior for the Al and Ga series are not due to incidental incorporation of Fe come from electrochemical behavior when Fe is intentionally incorporated: addition of 1% Fe content during fabrication of 5% Ga and 10% Ga electrodes induces the characteristic decrease in Tafel slope for electrocatalytic OER, as does the analysis of a 15% Ga electrode analyzed in a 1 M KOH solution that had not been subjected to the purification procedure (Figure S4). XPS measurements on 20% Ga and 20% Al samples before and after the electrochemical testing protocol show that Al-containing samples are compositionally stable while 80% of Ga is lost from the surface of the material during the 8-hour electrochemical testing protocol; measurements repeated after argon sputtering show that subsurface layers lost *ca.* 40% Ga (Figure S3). The anodic and cathodic redox peaks shift cathodically during the first 5 voltammetric cycles for Ga-Ni samples, after which the voltammetric behavior is stable even after extended electrochemical testing (Figure S5). Continued observation of a composition-dependent shift in the pre-catalytic redox process in the equilibrated samples suggests that while Ga rapidly dissolves from the surface during initial cycling, it does attain a functionally stable state and continues to affect the electrochemical behavior.

Synchrotron-based studies have been indispensable in revealing the bonding structure for disordered metal (oxy)hydroxides such as those studied here,<sup>41–45</sup> but limited accessibility to suitable facilities inhibits research progress. Such studies have consistently indicated that nickel (oxy)hydroxide materials possess a defective layered structure comprised of exclusively of bis- $\mu$ -(hydr)oxo Ni-M motifs, even after incorporation of secondary transition metal ions.<sup>28,31,37</sup> This consistency makes  $\text{M}_y\text{Ni}_{100-y}\text{O}_x$  an effective family on which to test alternative characterization techniques. Transition metal ions in an octahedral environment experience a splitting of *d*-orbitals to yield a  $t_{2g} e_g$  electron configuration, but a trigonal distortion of the nickel coordination environment is known for both well-crystallized  $\beta$ -Ni(OH)<sub>2</sub> and disordered Fe-Ni oxyhydroxide.<sup>28,46</sup> The resultant  $D_{3d}$  symmetry of Ni coordination environments is expected to split the triply degenerate  $t_{2g}$  orbitals into a non-degenerate orbital,  $a_{1g}$ , and a doubly degenerate set of orbitals,  $e_g$ , yielding a broad *d-d* transition at *ca.* 9000 cm<sup>-1</sup>.<sup>46–48</sup> All  $\text{M}_y\text{Ni}_{100-y}\text{O}_x$  films exhibit a broad absorbance band at approximately 9000 cm<sup>-1</sup> and a sharp band at approximately 6000



cm<sup>-1</sup> when in the reduced state (Figures 2A and S6). Upon electrochemical oxidation the high energy feature splits into two well-resolved bands and the low energy band experiences a red shift and grows in relative intensity (Figures 2B and S6). We assign the high energy bands to the two distinct *d-d* transitions expected for the *D*<sub>3d</sub> coordination environment (Figure 2C). A broad absorbance band between 6000 and 7800 cm<sup>-1</sup> was previously assigned as a second harmonic of the fundamental O-H vibration in nickel-containing layered double hydroxides.<sup>49,50</sup> The low energy feature is orders of magnitude more intense than the O-H vibrations in the materials studied here and exhibits a dependency on nickel oxidation state (Figure S7), however, ruling out assignment as a vibrational overtone.

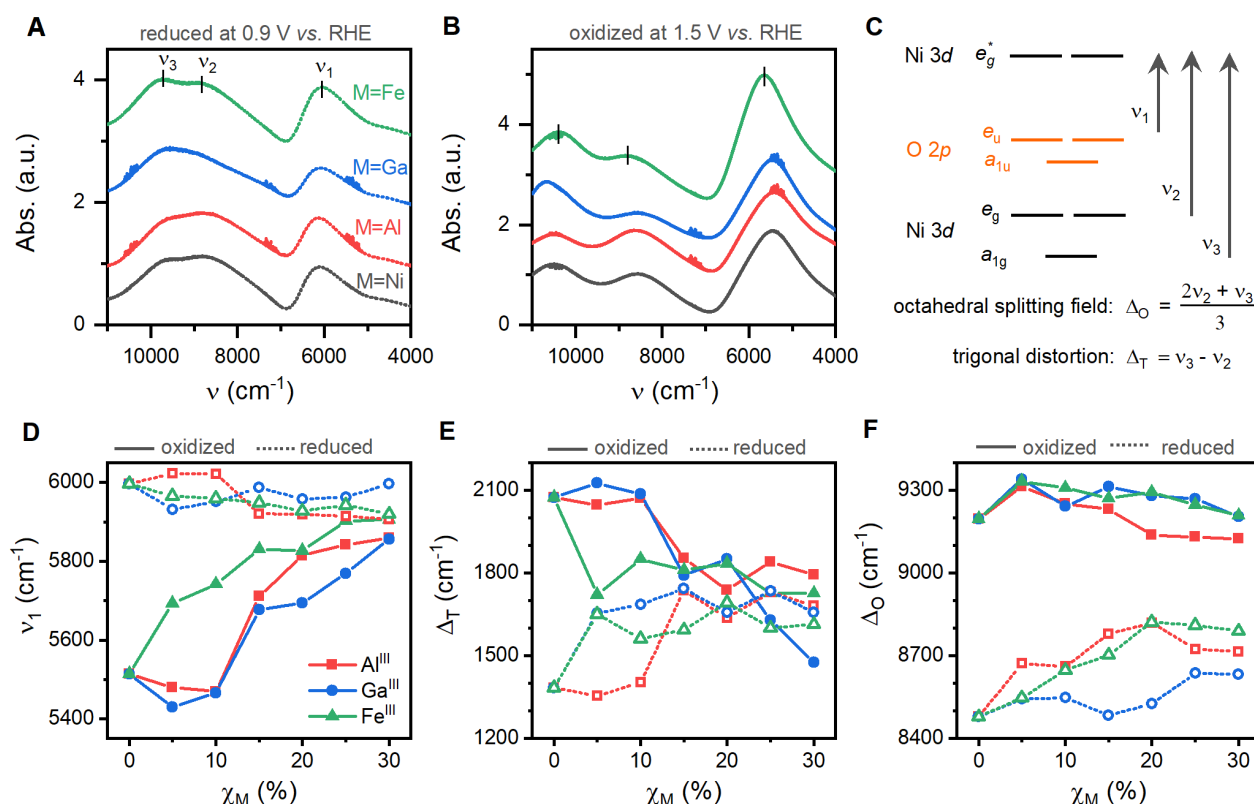


**Figure 2.** Near infrared spectra of  $M_{10}Ni_{90}O_x$ . Spectra for (A) the electrochemically reduced (B) and the electrochemically oxidized phases for  $M$  being Fe, Ga, Al and Ni. The (C) proposed electronic structure and assignments for absorbance processes are employed to track (D) the location of the low energy absorbance, (E) the splitting due to trigonal distortion, and (F) the octahedral splitting field as a function of relative stoichiometry for each composition series.

Projected density of states (PDOS; Figure 3) plots from DFT calculations on both the reduced and oxidized states show orbitals with Ni  $d_{z^2}$  character to be lowest in energy. Orbitals with character of the remaining Ni  $d$ -orbitals are split into two degenerate sets: an  $e_g$  located slightly above the  $d_{z^2}$  orbitals and an  $e_g^*$  above the Fermi level. (Figures 3 and S8-S10). Orbitals with O  $2p$  character are located between the  $e_g$  and  $e_g^*$  orbitals. These calculations lead us to tentatively assign  $\nu_1$  as a charge transfer process (Figure 2C). The consistency with past reports for  $\beta$ -Ni(OH)<sub>2</sub>,<sup>47</sup> the molecular orbital ordering indicated by DFT models (Figure 3), and recent reports detailing the splitting of nickel  $d$ -orbitals in

LaNiO<sub>3</sub> by bi-axial strain<sup>16</sup> bolster confidence in these assignments. The nickel *d-d* transitions in the NIR region therefore confirm a trigonal distortion of nickel coordination environments in all samples.

Comparison of the composition-dependent trends in the NIR spectra with DFT-generated models provides insight into the influence of Al, Ga and Fe on the bonding framework and electronic structure of the host Ni(OH)<sub>x</sub> material. The location of  $\nu_1$  shows the location of orbitals with oxygen 2*p* character relative to Ni-based  $e_g^*$  orbitals as a function of material composition (Figure 2D), the spacing between  $\nu_2$  and  $\nu_3$  approximates the magnitude of *d*-orbital splitting due to the trigonal distortion ( $\Delta_T$ ; Figure 2E), and the weighted average of  $\nu_2$  and  $\nu_3$  yields the octahedral splitting field ( $\Delta_O$ ; Figure 2F). In the reduced state,  $\nu_1$  decreases slightly while  $\Delta_T$  and  $\Delta_O$  increase with M-content for each composition series; in the oxidized state,  $\nu_1$  increases,  $\Delta_T$  decreases, and  $\Delta_O$  slightly decreases. By defining and varying the unit cell size, DFT calculations provide insight into the effects of compressive or tensile lattice strain on the electronic structure of the reduced and oxidized forms of nickel hydroxide, respectively. These calculations indicate that tensile strain on the oxidized state destabilizes the  $a_{1g}$  orbitals and stabilizes the  $e_g^*$  orbitals (Figure 3B). In contrast, compressive strain on the reduced state has little effect on the  $a_{1g}$  orbitals and slightly destabilizes the  $e_g$  and  $e_g^*$  orbitals (Figure 3A). Agreement between the computationally predicted trends and the experimentally observed ones support the assertion that the incorporation of suitably sized cations into the Ni(OH)<sub>2</sub> lattice influences electronic structure by modulating geometric strain.

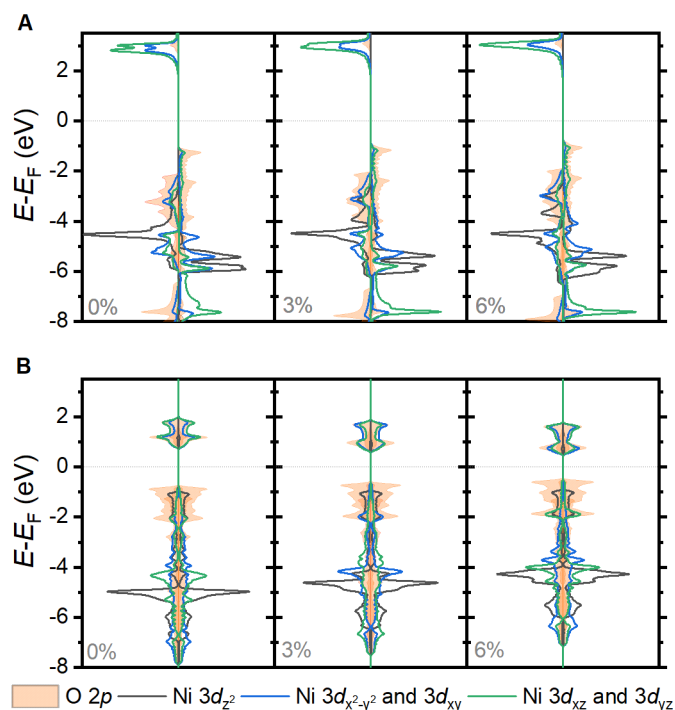


**Figure 3.** The influence of strain on the projected density of states for nickel oxyhydroxide. PDOS are shown for 0, 3 and 6% (A) compressive strain on the reduced phase and (B) tensile strain on the oxidized phase.

Reaction coordinate diagrams generated from the above DFT calculations provide a microscopic description for the observed changes in electrochemical behavior. The Butler-Volmer approach to analyzing electron transfer kinetics positions potential energy surfaces (PES) for the oxidized and

reduced phases on a suitable reaction coordinate. Application of a voltage changes the kinetic rate constants for the electron transfer reaction by stabilizing or destabilizing one PES curve relative to the other. Two parameters are required to mathematically describe electron transfer kinetics: the standard rate constant ( $k^0$ ) is defined by the activation energy at the standard reduction potential, and the transfer coefficient ( $\alpha$ ) is the magnitude of voltage-induced change to the cathodic rate constant relative to the applied overpotential. We generate PES diagrams for the oxidized and reduced states by varying cell dimensions for the slab used in DFT calculations (Figure 4A). The average Ni-M distance ( $R_{\text{Ni-M}}$ ) in *bis*- $\mu$ -(hydr)oxo structural motifs within the slab is used as the reaction coordinate because the  $\text{Ni}(\text{OH})_2$  lattice is known to contract upon oxidation and expand upon reduction; the parabola arising from mathematical fits of the computed stabilities are shifted to position their minima at zero energy, as would be observed at the standard reduction potential. An additional PES that simulates the application of a 300 mV overpotential is also shown in Figure 4A. These diagrams predict that  $R_{\text{Ni-M}}$  is linearly correlated to the effective ionic radii of the additive metals in both the reduced and oxidized phases (Figure 4B). The ionic radius mismatch brings the PES curves closer together on the reaction coordinate, effectively inducing a decrease in activation energy for electron transfer (Figure 4C). Repeating the computations with  $\text{In}^{\text{III}}$  as a significantly larger dopant predicts that the lattice will expand for both the oxidized and reduced states, inducing an increase in activation energy (Figure S11). This computational model suggests that the decrease in activation energy is unique to dopants with an ionic radius between those of the oxidized and reduced forms of nickel. Attempts to experimentally confirm the prediction were impeded by an inability to synthesize a Ni-In composition series. The relative shape of the PES curves remains essentially unchanged for Al and Ga dopants, but the oxidized PES broadens substantially for Fe. This asymmetric change results in a decrease in  $\alpha$  (Figure 4D). Such a change would favor oxidation reactions by making changes in affect the anodic rate constant more significantly than the cathodic rate constant. This analysis predicts that the incorporation of ions with a radius between  $\text{Ni}^{\text{II}}$  and  $\text{Ni}^{\text{IV}}$  into a  $\text{Ni}(\text{OH})_2$  lattice will decrease the activation energy for electron transfer, and decrease the electron transfer coefficient by asymmetrically distorting the PES once beyond a certain threshold.

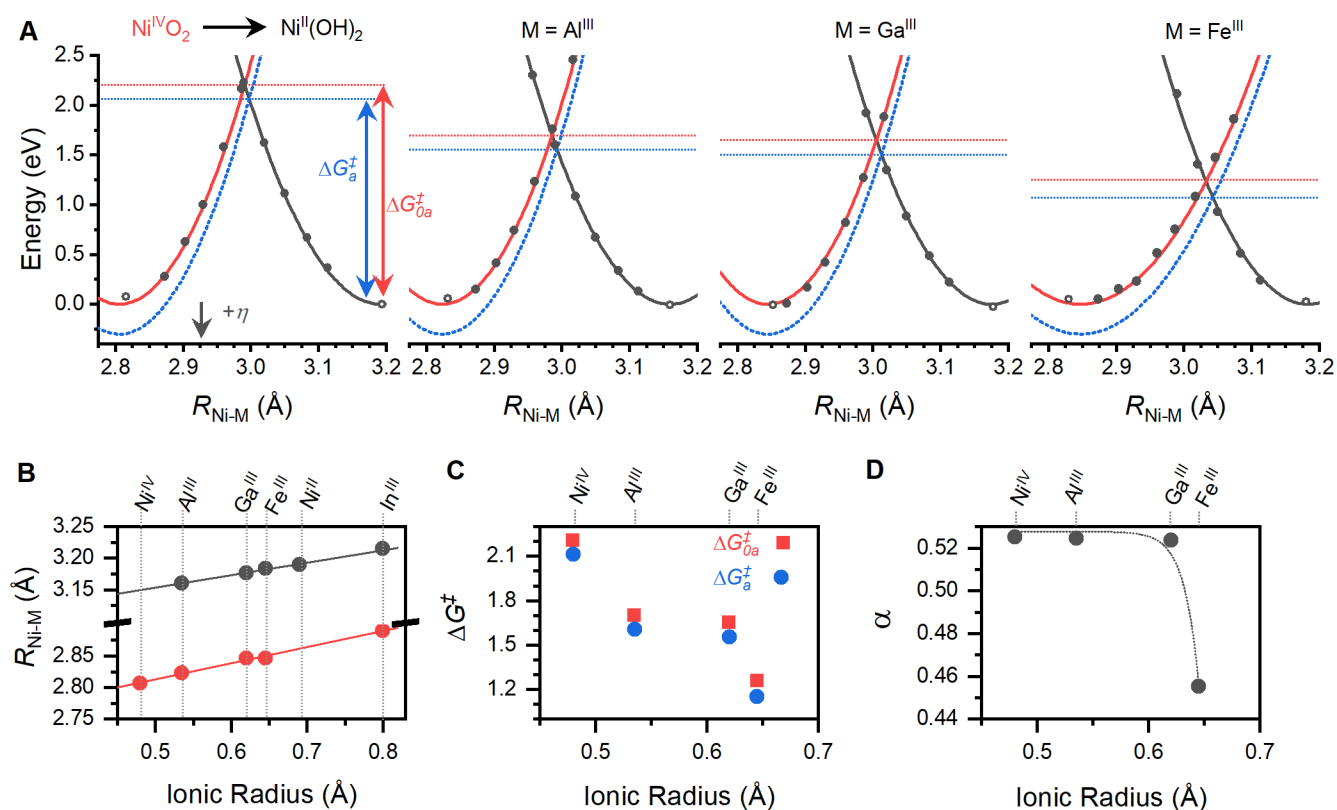


**Figure 4.** Reaction coordinate diagrams and parameters for electron transfer kinetics for M-containing nickel oxyhydroxide. (A) Potential energy surfaces as a function of the Ni-M distance in bis- $\mu$ -oxo Ni-M structural motifs for the reduced phase (red curves) and the oxidized phase at overpotentials of 0 V (black curves) and 0.3 V (blue curves) for M being  $\text{Ni}^{\text{II/IV}}$ ,  $\text{Al}^{\text{III}}$ ,  $\text{Ga}^{\text{III}}$ ,  $\text{Fe}^{\text{III}}$ . Variable-cell relaxation results are indicated by the hollow data point. (B) The energy minima from the potential energy surface parabola, (C) activation energies for electrochemical oxidation, (D) and the electrochemical transfer coefficient are given as a function of the effective bond length of the dopant metal.

## DISCUSSION

The agreement between trends in DFT models and experimental results suggest that the addition of selected cations, namely  $\text{Al}^{\text{III}}$ ,  $\text{Ga}^{\text{III}}$  and  $\text{Fe}^{\text{III}}$ , to a nickel hydroxide lattice can be structurally modeled by limiting the extent to which the host nickel hydroxide lattice can expand and contract. A static Fe-O bond distance in  $\text{Fe}_y\text{Ni}_{100-y}\text{O}_x$  was previously shown to reside between that of  $\text{Ni}^{\text{II}}\text{-O}$  and  $\text{Ni}^{\text{IV}}\text{-O}$  at voltages up to 1.6 V vs. RHE,<sup>28</sup> effectively distorting the structure by inhibiting the oxidative compression and reductive expansion of the host nickel hydroxide lattice. The DFT models generated here predict that the Ni-M distance and O-Ni-O bond angles in bis- $\mu$ -(hydr)oxo motifs are influenced by the effective ionic radius of the secondary metal ion (Figures 4B and 5A). The PDOS diagrams in Figure 3 indicate that tensile strain in the oxidized state of  $\text{Ni}(\text{OH})_2$  would decrease both the octahedral splitting field ( $\Delta_{\text{O}}$ ) and the trigonal distortion ( $\Delta_{\text{T}}$ ); an increase in both parameters would arise from compressive strain in the reduced state. The NIR spectra show composition dependent trends in both  $\Delta_{\text{O}}$  and  $\Delta_{\text{T}}$  that match this predicted behavior, suggesting that the additive metals increase internal strain within the  $\text{M}_y\text{Ni}_{100-y}\text{O}_x$  materials (Figure 2).

The similarity in anodic shift rate for redox peaks in all composition series provides clear evidence that the pre-catalytic redox process is fundamentally decoupled from electrocatalysis. The consistency of anodic shift rate for all composition series in spite of variable electronegativity for each of the additive metals suggests that inductive effects or changes in Ni-O bond strength are not responsible for the behavioral change. The predicted linear relationship between effective ionic radii and average  $R_{\text{Ni-M}}$  in bis- $\mu$ -(hydr)oxo motifs shown in Figure 4D suggests that the overall strain present in the system may be the key consideration underlying this behavioral feature. It is well established that the oxidation of  $\text{Ni}(\text{OH})_2$  induces a reversible contraction in  $R_{\text{Ni-M}}$ ,<sup>25,28,31,32,44</sup> the models here predict a decrease in the magnitude of this contraction when secondary metals are incorporated. As the thermodynamics for an electron transfer reaction are based on the energetics of both the oxidized and reduced states, we propose that the opposing strain present in the oxidized and reduced states is responsible for the anodic shift. Such an interpretation is supported by the observed shift of redox processes when shape-memory alloys have been used to apply compressive or tensile strain,<sup>17,18</sup> and when elastomer substrates have been used to apply a gradient of tensile strain.<sup>11</sup> The assignment is also in line with past work on metal alloys, where the  $d$ -band of pseudomorphic monolayers has been shown to be destabilized by tensile strain and stabilized by compressive strain.<sup>13,14</sup> This strain-induced effect has been shown to shift electrochemical redox processes cathodically when compressive strain is applied, and anodically when tensile strain is applied.<sup>15</sup>

The results here suggest that the pre-catalytic process is highly dependent on the total strain within the material while the catalytic process is either decoupled from strain or presents a non-linear correlation that cannot be discerned from the present dataset. A decrease in Tafel slope is the primary catalytic change observed following incorporation of Fe into nickel hydroxide. Experimentally observed Tafel slopes are a function of reaction mechanism and identity of the rate limiting step:<sup>51,52</sup> rate-limiting steps involving electron transfer present a Tafel slope that is scaled by  $\alpha$  for that reaction, chemical steps present as constant slopes,<sup>51,52</sup> and pushing the rate-limiting step later in a catalytic cycle results in a decreased Tafel slope (in  $\text{mV dec}^{-1}$ ). The step-wise change observed for the Fe-Ni composition series implies either a shifting of the rate-limiting step later in the catalytic cycle or a change in dominant reaction mechanism. The gradual change in Tafel slope following incorporation of Ga or Al suggests that the rate limiting step for OER in these samples is an electron transfer step rather than a chemical reaction. The assumption that the trends in our computational model apply to catalytically relevant sites leads to the conclusion that there is either (i) a threshold of strain to trigger the behavior observed in the Fe-Ni case, which is alluded to by the PES distortions captured in Figure 4D, (ii) the  $d$ -orbitals in Fe enable a synergistic combination of geometric strain and bonding effects in the Fe-Ni series, or (iii) a secondary reaction mechanism such as the electrochemical oxidation of  $\text{Fe}^{\text{III}}$  to higher oxidation states becomes dominant.<sup>25,26</sup> We note that previous systematic studies on cation dopants such as Ti, Mn and Co into nickel hydroxide lattices have not revealed any correlations in pre-catalytic behavior with comparable Fe-Ni compositions.<sup>24,53</sup> The correlations reported here for Al-Ni, Ga-Ni and Fe-Ni thus confirm the need for the selection criteria discussed earlier to study the type of internalized geometric lattice strain analyzed here. These criteria provide an unfortunate limit on the number of elements suitable for use in replicating the catalytic properties of the Fe-Ni materials through simple compositional tuning. The development of tunable substrate based approaches, such as those based on shape-memory alloys,<sup>17,18</sup> may provide a means to overcome this limitation.

## CONCLUSIONS

We have studied binary Al-Ni, Ga-Ni and Fe-Ni hydroxides to explore the role of internalized geometric strain on electrocatalytic water oxidation by nickel hydroxide-based materials. The Al-Ni and Ga-Ni series replicate the well-documented composition-dependent anodic shift of the pre-catalytic redox process for the Fe-Ni series, but did not significantly influence electrocatalytic water oxidation. Near infrared spectroscopy and DFT models provide evidence that asymmetric distortions in the oxidized and reduced states can be achieved by the incorporation of cations with a suitable ionic radius into a nickel-based lattice. The computational models indicate that all three composition series shift the potential energy surfaces to decrease the activation energy barrier for oxidation of nickel sites, but that only Fe significantly alters the electrochemical transfer coefficient that would manifest as lower Tafel slopes. We attribute the composition-dependent anodic shift of pre-catalytic redox processes in nickel hydroxide materials to asymmetric strain in the oxidized and reduced states of the nickel hydroxide lattice. Failure to emulate the electrocatalytic performance of Fe-Ni hydroxides using other compositions suggests that geometric strain is not solely responsible for improved catalysis.

## ASSOCIATED CONTENT

**Supporting Information.** Voltammetric results for pure samples and intentionally contaminated samples, sample chronoamperometric results, X-ray photoelectron spectra, near infrared spectra, energy and optimized structures from DFT calculations, projected density of states for subset of Al-Ni, Ga-Ni and Fe-Ni samples, reaction coordinates for  $[\text{InNi}_8\text{O}(\text{OH})_{17}]$  and  $[\text{InNi}_8\text{O}_{18}]^-$ . This material is available free of charge via the Internet at <http://pubs.acs.org>.

## AUTHOR INFORMATION

**Corresponding Author.** [rodsmith@uwaterloo.ca](mailto:rodsmith@uwaterloo.ca)

**Present Address.** Department of Chemistry, University of Waterloo, 200 University Avenue W., Waterloo, Ontario, Canada N2L 3G1

**Author Contributions.** The manuscript was written through contributions of all authors.

**Funding Sources.** This research was supported by funds from the Natural Sciences and Engineering Research Council (NSERC) Discovery Grant program.

## ACKNOWLEDGEMENTS

We thank Compute Canada and the Shared Hierarchical Academic Research Computing Network (SHARCNET) for computing resources and Waterloo Advanced Technology Laboratory for instrumentation access.

## REFERENCES

- (1) Greeley, J.; Jaramillo, T. F.; Bonde, J.; Chorkendorff, I.; Nørskov, J. K. Computational High-Throughput Screening of Electrocatalytic Materials for Hydrogen Evolution. *Nat. Mater.* **2006**, *5*, 909–913.
- (2) Vojvodic, A.; Nørskov, J. K. New Design Paradigm for Heterogeneous Catalysts. *Nat. Sci. Rev.* **2015**, *2*, 140–149.
- (3) She, Z. W.; Kibsgaard, J.; Dickens, C. F.; Chorkendorff, I.; Nørskov, J. K.; Jaramillo, T. F. Combining Theory and Experiment in Electrocatalysis: Insights into Materials Design. *Science* **2017**, *355*, eaad4998.
- (4) Suntivich, J.; May, K. J.; Gasteiger, H. A.; Goodenough, J. B.; Shao-Horn, Y. A Perovskite Oxide Optimized for Oxygen Evolution Catalysis from Molecular Orbital Principles. *Science* **2011**, *334*, 1383–1385.
- (5) Seitz, L. C.; Dickens, C. F.; Nishio, K.; Hikita, Y.; Montoya, J.; Doyle, A.; Kirk, C.; Vojvodic, A.; Hwang, H. Y.; Nørskov, J. K.; et al. A Highly Active and Stable IrO<sub>x</sub>/SrIrO<sub>3</sub> Catalyst for the Oxygen Evolution Reaction. *Science* **2016**, *353*, 1011–1014.
- (6) Smith, R. D. L.; Prévot, M. S.; Fagan, R. D.; Zhang, Z.; Sedach, P. A.; Siu, M. K. J.; Trudel, S.; Berlinguette, C. P. Photochemical Route for Accessing Amorphous Metal Oxide Materials for Water Oxidation Catalysis. *Science* **2013**, *340*, 60–63.
- (7) Kanan, M. W.; Nocera, D. G. In Situ Formation of an Oxygen-Evolving Catalyst in Neutral Water Containing Phosphate and Co<sup>2+</sup>. *Science* **2008**, *321*, 1072–1075.
- (8) Bergmann, A.; Martinez-Moreno, E.; Teschner, D.; Chernev, P.; Gliech, M.; de Araújo, J. F.; Reier, T.; Dau, H.; Strasser, P. Reversible Amorphization and the Catalytically Active State of Crystalline Co<sub>3</sub>O<sub>4</sub> during Oxygen Evolution. *Nat. Commun.* **2015**, *6*, 8625.
- (9) Risch, M.; Grimaud, A.; May, K. J.; Stoerzinger, K. A.; Chen, T. J.; Mansour, A. N.; Shao-Horn, Y. Structural Changes of Cobalt-Based Perovskites upon Water Oxidation Investigated by EXAFS. *J. Phys. Chem. C* **2013**, *117*, 8628–8635.
- (10) May, K. J.; Carlton, C. E.; Stoerzinger, K. A.; Risch, M.; Suntivich, J.; Lee, Y.-L.; Grimaud, A.; Shao-Horn, Y. Influence of Oxygen Evolution during Water Oxidation on the Surface of Perovskite Oxide Catalysts. *J. Phys. Chem. Lett* **2012**, *3*, 3264–3270.
- (11) Li, H.; Tsai, C.; Koh, A. L.; Cai, L.; Contryman, A. W.; Fragapane, A. H.; Zhao, J.; Han, H. S.; Manoharan, H. C.; Abild-Pedersen, F.; et al. Activating and Optimizing MoS<sub>2</sub> Basal Planes for Hydrogen Evolution through the Formation of Strained Sulphur Vacancies. *Nat. Mater.* **2016**, *15*, 48–53.
- (12) Rodriguez, J. A.; Goodman, D. W. The Nature of the Metal-Metal Bond in Bimetallic Surfaces. *Science* **1992**, *257*, 897–903.
- (13) Hammer, B.; Nørskov, J. K. Electronic Factors Determining the Reactivity of Metal Surfaces. *Surf. Sci.* **1995**, *343*, 211–220.
- (14) Ruban, A.; Hammer, B.; Stoltze, P.; Skriver, H. L.; Nørskov, J. K. Surface Electronic Structure and Reactivity of Transition and Noble Metals. *J. Mol. Catal. A Chem.* **1997**, *115*, 421–429.
- (15) Kibler, L. A.; El-Aziz, A. M.; Hoyer, R.; Kolb, D. M. Tuning Reaction Rates by Lateral Strain in a Palladium Monolayer. *Angew. Chemie - Int. Ed.* **2005**, *44* (14), 2080–2084.

- (16) Petrie, J. R.; Cooper, V. R.; Freeland, J. W.; Meyer, T. L.; Zhang, Z.; Lutterman, D. A.; Lee, H. N. Enhanced Bifunctional Oxygen Catalysis in Strained  $\text{LaNiO}_3$  Perovskites. *J. Am. Chem. Soc.* **2016**, *138*, 2488–2491.
- (17) Du, M.; Cui, L.; Cao, Y.; Bard, A. J. Mechanoelectrochemical Catalysis of the Effect of Elastic Strain on a Platinum Nanofilm for the ORR Exerted by a Shape Memory Alloy Substrate. *J. Am. Chem. Soc.* **2015**, *137*, 7397–7403.
- (18) Muralidharan, N.; Carter, R.; Oakes, L.; Cohn, A. P.; Pint, C. L. Strain Engineering to Modify the Electrochemistry of Energy Storage Electrodes. *Sci. Rep.* **2016**, *6*, 27542.
- (19) Chattot, R.; Le Bacq, O.; Beermann, V.; Kühn, S.; Herranz, J.; Henning, S.; Kühn, L.; Asset, T.; Guétaz, L.; Renou, G.; et al. Surface Distortion as a Unifying Concept and Descriptor in Oxygen Reduction Reaction Electrocatalysis. *Nat. Mater.* **2018**, *17*, 827–833.
- (20) Smith, R. D. L.; Prévot, M. S.; Fagan, R. D.; Trudel, S.; Berlinguette, C. P. Water Oxidation Catalysis: Electrocatalytic Response to Metal Stoichiometry in Amorphous Metal Oxide Films Containing Iron, Cobalt, and Nickel. *J. Am. Chem. Soc.* **2013**, *135*, 11580–11586.
- (21) Louie, M. W.; Bell, A. T. An Investigation of Thin-Film Ni-Fe Oxide Catalysts for the Electrochemical Evolution of Oxygen. *J. Am. Chem. Soc.* **2013**, *135*, 12329–12337.
- (22) Trotochaud, L.; Young, S. L.; Ranney, J. K.; Boettcher, S. W. Nickel–Iron Oxyhydroxide Oxygen-Evolution Electrocatalysts: The Role of Intentional and Incidental Iron Incorporation. *J. Am. Chem. Soc.* **2014**, *136*, 6744–6753.
- (23) Corrigan, D. A. The Catalysis of the Oxygen Evolution Reaction by Iron Impurities in Thin Film Nickel Oxide Electrodes. *J. Electrochem. Soc.* **1987**, *134* (2), 377–384.
- (24) Corrigan, D. A.; Bendert, R. M. Effect of Coprecipitated Metal Ions on the Electrochemistry of Nickel Hydroxide Thin Films: Cyclic Voltammetry in 1M KOH. *J. Electrochem. Soc.* **1989**, *136* (89), 723–728.
- (25) Friebe, D.; Louie, M. W.; Bajdich, M.; Sanwald, K. E.; Cai, Y.; Wise, A. M.; Cheng, M.-J.; Sokaras, D.; Weng, T.-C.; Alonso-Mori, R.; et al. Identification of Highly Active Fe Sites in  $(\text{Ni,Fe})\text{OOH}$  for Electrocatalytic Water Splitting. *J. Am. Chem. Soc.* **2015**, *137*, 1305–1313.
- (26) Hunter, B. M.; Thompson, N. B.; Müller, A. M.; Rossman, G. R.; Hill, M. G.; Winkler, J. R.; Gray, H. B. Trapping an Iron(VI) Water-Splitting Intermediate in Nonaqueous Media. *Joule* **2018**, *2*, 747–763.
- (27) Li, N.; Bediako, D. K.; Hadt, R. G.; Hayes, D.; Kempa, T. J.; von Cube, F.; Bell, D. C.; Chen, L. X.; Nocera, D. G. Influence of Iron Doping on Tetravalent Nickel Content in Catalytic Oxygen Evolving Films. *Proc. Natl. Acad. USA* **2017**, *114*, 1486–1491.
- (28) Smith, R. D. L.; Pasquini, C.; Loos, S.; Chernev, P.; Klingan, K.; Kubella, P.; Mohammadi, M. R.; González-Flores, D.; Dau, H. Geometric Distortions in Nickel (Oxy)Hydroxide Electrocatalysts by Redox Inactive Iron Ions. *Energy Environ. Sci.* **2018**, *11*, 2476–2485.
- (29) Chen, J. Y. C.; Dang, L.; Liang, H.; Bi, W.; Gerken, J. B.; Jin, S.; Alp, E. E.; Stahl, S. S. Operando Analysis of NiFe and Fe Oxyhydroxide Electrocatalysts for Water Oxidation: Detection of  $\text{Fe}^{4+}$  by Mössbauer Spectroscopy. *J. Am. Chem. Soc.* **2015**, *137*, 15090–15093.
- (30) Goldsmith, Z. K.; Harshan, A. K.; Gerken, J. B.; Vörös, M.; Galli, G.; Stahl, S. S.; Hammes-



- Schiffer, S. Characterization of NiFe Oxyhydroxide Electrocatalysts by Integrated Electronic Structure Calculations and Spectroelectrochemistry. *Proc. Natl. Acad. USA* **2017**, *114* (12), 3050–3055.
- (31) Görlin, M.; Chernev, P.; Araujo, F. J.; Reier, T.; Dresch, S.; Paul, B.; Krähnert, R.; Dau, H.; Strasser, P. Oxygen Evolution Reaction Dynamics, Faradaic Charge Efficiency, and the Active Metal Redox States of Ni–Fe Oxide Water Splitting Electrocatalysts. *J. Am. Chem. Soc.* **2016**, *138*, 5603–5614.
- (32) Gonzalez-Flores, D.; Klingan, K.; Chernev, P.; Loos, S.; Mohammadi, M. R.; Pasquini, C.; Kubella, P.; Zaharieva, I.; Smith, R. D. L.; Dau, H. Nickel-Iron Catalysts for Electrochemical Water Oxidation – Redox Synergism Investigated by in Situ X-Ray Spectroscopy with Millisecond Time Resolution. *Sustain. Energy Fuels* **2018**, *2*, 1986.
- (33) Corrigan, D. A.; Knight, S. L. Electrochemical and Spectroscopic Evidence on the Participation of Quadrivalent Nickel in the Nickel Hydroxide Redox Reaction. *J. Electrochem. Soc.* **1989**, *136*, 613–619.
- (34) Giannozzi, P.; Baroni, S.; Bonini, N.; Calandra, M.; Car, R.; Cavazzoni, C.; Ceresoli, D.; Chiarotti, G. L.; Cococcioni, M.; Dabo, I.; et al. QUANTUM ESPRESSO: A Modular and Open-Source Software Project for Quantum Simulations of Materials. *J. Phys. Condens. Matter* **2009**, *21*, 395502.
- (35) Chakrapani, K.; Özcan, F.; Ortega, K. F.; Machowski, T.; Behrens, M. Composition-Dependent Effect of the Calcination of Cobalt-, Nickel-, and Gallium-Based Layered Double Hydroxides to Mixed Metal Oxides in the Oxygen Evolution Reaction. *ChemElectroChem* **2018**, *5* (1), 93–100.
- (36) Evans, D. G.; Slade, R. C. T. Structural Aspects of Layered Double Hydroxides. *Struct. Bond.* **2006**, *119*, 1–87.
- (37) Arias, S.; Eon, J. G.; Gil, R. A. S. S.; Licea, Y. E.; Palacio, L. A.; Farooj, A. C. Synthesis and Characterization of Terephthalate-Intercalated NiAl Layered Double Hydroxides with High Al Content. *Dalt. Trans.* **2013**, *42*, 2084–2093.
- (38) Shannon, R. D. Revised Effective Ionic Radii and Systematic Studies of Interatomic Distances in Halides and Chalcogenides. *Acta Cryst* **1976**, *32*, 751–767.
- (39) Enman, L.; Burke Stevens, M.; Dahan, M.; Nellist, M.; Caspary Toroker, M.; Boettcher, S. W. Operando X-Ray Absorption Spectroscopy Shows Fe Oxidation Is Concurrent with Oxygen Evolution in Cobalt-Iron (Oxy)Hydroxide Electrocatalysts. *Angew. Chem. Int. Ed.* **2018**, *57*, 12840–12844.
- (40) Lyons, M. E. G.; Brandon, M. P. The Oxygen Evolution Reaction on Passive Oxide Covered Transition Metal Electrodes in Aqueous Alkaline Solution. Part 1-Nickel. *Int. J. Electrochem. Sci* **2008**, *3*, 1386–1424.
- (41) Risch, M.; Khare, V.; Zaharieva, I.; Gerencser, L.; Chernev, P.; Dau, H. Cobalt-Oxo Core of a Water-Oxidizing Catalyst Film. *J. Am. Chem. Soc.* **2009**, *131*, 6936–6937.
- (42) Risch, M.; Klingan, K.; Heidkamp, J.; Ehrenberg, D.; Chernev, P.; Zaharieva, I.; Dau, H. Nickel-Oxide Structure of a Water-Oxidizing Catalyst Film. *Chem. Commun.* **2011**, *47*, 11912–11914.
- (43) Kanan, M. W.; Yano, J.; Surendranath, Y.; Dincă, M.; Yachandra, V. K.; Nocera, D. G. Structure and Valency of a Cobalt-Phosphate Water Oxidation Catalyst Determined by in Situ X-Ray

- Spectroscopy. *J. Am. Chem. Soc.* **2010**, *132*, 13692–13701.
- (44) Bediako, D. K.; Lassalle-Kaiser, B.; Surendranath, Y.; Yano, J.; Yachandra, V. K.; Nocera, D. G. Structure–Activity Correlations in a Nickel–Borate Oxygen Evolution Catalyst. *J. Am. Chem. Soc.* **2012**, *134*, 6801–6809.
- (45) Smith, R. D. L.; Pasquini, C.; Loos, S.; Chernev, P.; Klingan, K.; Kubella, P.; Mohammadi, M. R.; Gonzalez-Flores, D.; Dau, H. Spectroscopic Identification of Active Sites for the Oxygen Evolution Reaction on Iron-Cobalt Oxides. *Nat. Commun.* **2017**, *8*, 2022.
- (46) Hall, D. S.; Lockwood, D. J.; Bock, C.; MacDougall, B. R. Nickel Hydroxides and Related Materials: A Review of Their Structures, Synthesis and Properties. *Proc. R. Soc. A* **2014**, *471*, 20140792.
- (47) Krehula, S.; Ristić, M.; Wu, C.; Li, X.; Jiang, L.; Wang, J.; Sun, G.; Zhang, T.; Perović, M.; Bošković, M.; et al. Influence of Fe(III) Doping on the Crystal Structure and Properties of Hydrothermally Prepared  $\beta$ -Ni(OH)<sub>2</sub> Nanostructures. *J. Alloys Compd.* **2018**, *750*, 687–695.
- (48) Bussiè, G.; Reber, C. Coupled Excited States in Nickel(II) Complexes Probed by Polarized Absorption Spectroscopy. *J. Am. Chem. Soc.* **1998**, *120*, 6306–6315.
- (49) Tao, Q.; Reddy, B. J.; He, H.; Frost, R. L.; Yuan, P.; Zhu, J. Synthesis and Infrared Spectroscopic Characterization of Selected Layered Double Hydroxides Containing Divalent Ni and Co. *Mater. Chem. Phys.* **2008**, *112*, 869–875.
- (50) Frost, R. L.; Ding, Z.; Klopogge, J. T. The Application of Near-Infrared Spectroscopy to the Study of Brucite and Hydrotalcite Structure. *Can. J. Anal. Sci. Spectrosc.* **2000**, *45* (4), 96–101.
- (51) O', J.; Bockris, M.; Otagawa, T. Mechanism of Oxygen Evolution on Perovskites. *J. Phys. Chem.* **1983**, *57*, 2960–2971.
- (52) Shinagawa, T.; Garcia-Esparza, A. T.; Takanabe, K. Insight on Tafel Slopes from a Microkinetic Analysis of Aqueous Electrocatalysis for Energy Conversion. *Sci. Rep.* **2015**, *5*, 13801.
- (53) Enman, L. J.; Burke, M. S.; Batchellor, A. S.; Boettcher, S. W. Effects of Intentionally Incorporated Metal Cations on the Oxygen Evolution Electrocatalytic Activity of Nickel (Oxy)Hydroxide in Alkaline Media. *ACS Catal.* **2016**, *6*, 2416–2423.

### Table of Contents Figure:

